

# Molecular dynamics study of hcp/fcc nucleation and growth in bcc iron driven by uniaxial strain

Baotian Wang,<sup>1,2</sup> Jianli Shao,<sup>2</sup> Guangcai Zhang,<sup>2</sup> Weidong Li,<sup>1</sup> and Ping Zhang<sup>2,3,\*</sup>

<sup>1</sup>*Institute of Theoretical Physics and Department of Physics, Shanxi University, Taiyuan 030006, People's Republic of China*

<sup>2</sup>*Institute of Applied Physics and Computational Mathematics, P.O. Box 8009, Beijing 100088, People's Republic of China*

<sup>3</sup>*Center for Applied Physics and Technology, Peking University, Beijing 100871, People's Republic of China*

(Dated: November 3, 2018)

Molecular dynamics simulations are performed to investigate the structural phase transition in body-centered cubic (bcc) single crystal iron under high strain rate loading. We study the nucleation and growth of the hexagonal-close-packed (hcp) and face-centered-cubic (fcc) phases, and their crystal orientation dependence. Results reveal that the transition pressures are less dependent on the crystal orientations ( $\sim 14$  GPa for loading along [001], [011], and [111] directions). However, the pressure interval of mixed phase for [011] loading is much shorter than loading along other orientations. And the temperature increased amplitude for [001] loading is evidently lower than other orientations. The hcp/fcc nucleation process is presented by the topological medium-range-order analysis. For loading along [001] direction, we find that the hcp structure occurs firstly and grows into laminar morphology in the  $(011)_{\text{bcc}}$  planes with a little fcc atoms as intermediate structure. For loading along [011] and [111] directions, both the hcp and fcc structures nucleation and growth along the  $\{110\}_{\text{bcc}}$  planes are observed, whose morphology is also discussed.

PACS numbers: 64.70.kd, 71.15.Pd, 61.50.Ks, 62.50.-p

## I. INTRODUCTION

Besides melting, dislocation generation, and twinning, structural phase transition is also one important physical process in understanding the plasticity of solid (metallic, particularly) materials. Among various metallic materials, iron, due to its critical importance in condensed-matter physics, materials science, geophysics, and human development, have been extensively studied in aiming at understanding its structures and phase transition under extreme conditions. Thereinto, the research on classical phase transition of iron from ferromagnetic body-centered cubic (bcc) ground state  $\alpha$  phase to nonmagnetic hexagonal-close-packed (hcp)  $\epsilon$  phase has a history of more than half a century. Early representative work was carried out in 1956 by Bancroft *et al.* [1], where they discovered the transition under shock wave compression at pressure around 13 GPa. Thereafter, plenty of theoretical and experimental works have been done to study the structure properties, inner physics, and mechanical features involving this  $\alpha \rightarrow \epsilon$  transition process [2, 3, 4, 5, 6, 7, 8]. Among these studies, in 1962, Jamieson and Lawson obtained crystallographic evidence for the  $\alpha \rightarrow \epsilon$  transition at 13 GPa in static x-ray diffraction experiments [2], which confirmed previous shock-wave experiment of Bancroft *et al.* [1]; in 1991, Taylor and Pasternak reported the onset of the transition in range of 9-15 GPa with a large hysteresis width of

about 6 GPa [4]; in 1997, Boettger and Wallace presented theoretical analysis of metastability and dynamics of the transition [6]; in 1999, Wang and Ingalls suggested three possible models for the  $\alpha \rightarrow \epsilon$  transition mechanism [7]; and in 2004, Caspersen *et al.* theoretically investigated the influence of shear in the transition based on a multi-scale model [8].

However, the structural transition is a mutation process, which leads to direct observation of the phase transition very difficult in experiment. And the abrupt changes in physical and mechanical characteristics also bring about difficulty in theoretically analyzing the dynamic response and micro-behavior of materials. Therefore, it is necessary to carry out systematic simulations at atomic level by using molecular dynamics (MD). MD is a method for computationally evaluating the thermodynamic and transport properties of materials by solving the classical equations of motion at the atomic level. Many preceding works have testified that MD is the most conceptually straightforward method and an altogether very utilitarian method for obtaining atomic details. In 2002, Kadau *et al.* [9] realized the micro-simulation of shock-induced phase transition of solid iron along [001] direction by employing MD method with an embedded atom method (EAM) potential [10, 11], showing the micro-features of  $\alpha \rightarrow \epsilon$  transition. Subsequent ultrafast x-ray diffraction experiments processed by Kalantar *et al.* [12] verified the validity of this work. In 2005, Kadau *et al.* [13] simulated shock-induced phase transformations in bcc iron induced by shock loading along [001], [011], and [111] directions to research the orientation dependence of the developing microstructure on the crystallographic shock direction. They found that the fcc phase appeared especially when

---

\*To whom correspondence should be addressed. E-mail: zhang\_ping@iapcm.ac.cn

loading along [011] and [111] directions. In 2007, Kadau *et al.* [14] utilized the MD method again to simulate the polycrystalline iron in shock loading condition, simulation results correspond properly with experiment [15].

These abovementioned MD studies have greatly enriched our knowledge of the structural transition of iron and, needless to say, subsequently inspired more simulation works [16, 17]. In our last work [17], we have simulated the  $\alpha \rightarrow \epsilon$  structural transition of iron under isothermal compression along the [001] direction. It was showed that the laminar structure forms along  $\{110\}_{\text{bcc}}$  planes. On the other hand, when the loading direction is different, both the hcp and fcc nucleation and growth in bcc single crystal iron will occur. To date, no detailed investigation has been proceeded to study the orientation dependence of hcp and fcc nucleation and growth. This issue is focus of our present paper. Specially, by adiabatic compression along [001], [011], and [111] directions, in this paper, we investigate the  $\alpha \rightarrow \epsilon/\gamma$  structural phase transition in bcc single crystal iron. The pressure and temperature effect, nucleation mechanism and morphology characters are all discussed.

The rest of this paper is arranged as follows. In Sec. II the simulation method is briefly described. In Sec. III we present and discuss our simulated results. A summary of our main results is given in Sec. IV.

## II. METHODOLOGY OF THE SIMULATIONS

For this work, we use classical MD and the EAM potential of iron developed by Voter-Chen (VC) [18] to conduct the simulations. Our calculations are performed in three cases by using three samples A, B, and C to simulate the loadings along the [001], [011], and [111], respectively. Specially, sample A consists of  $50_{x,[100]} \times 50_{y,[010]} \times 100_{z,[001]}$  atomic cells, sample B consists of  $36_{x,[011]} \times 100_{y,[\bar{1}00]} \times 72_{z,[0\bar{1}1]}$  cells, and sample C consists of  $36_{x,[\bar{1}10]} \times 40_{y,[\bar{1}\bar{1}2]} \times 180_{z,[111]}$  cells. Periodical boundary conditions are adopted in all directions. The original temperature in all samples is set at 60 K by speed calibration method [19]. The initial state is manipulated at zero pressure through modulating the lattice constant. Here the lattice constant of all samples is  $a_0=0.28725$  nm. Loading with high strain rate of  $\sim 10^8$  along the [001], [011], and [111] directions is implemented by shortening the lattice constants of these three orientations step by step during the nonequilibrium MD process. The Verlet algorithm [20] is used to integrate the equation of motion. The simulation time is up to 200 ps, with the time step set at 2 fs. Special techniques are required to analyze the huge amount of data produced in the MD simulations. Here, the local structure around each atom are resolved by using the topological medium-range-order analysis [21] technique. The phase mass fraction analysis and radial distribution function are also presented to obtain the phase transition information.

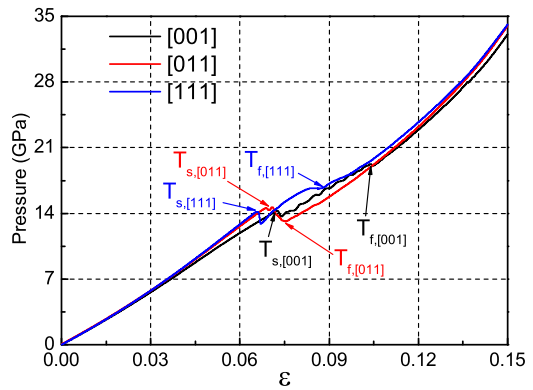


FIG. 1: (Color online) Variation of pressure with the strain  $\epsilon$  for loading along [001], [011], and [111] directions. The mixed phase intervals start at  $T_{s,[001]}$ (0.072, 14.21),  $T_{s,[011]}$ (0.071, 14.66), and  $T_{s,[111]}$ (0.066, 14.16) and finish at  $T_{f,[001]}$ (0.104, 19.25),  $T_{f,[011]}$ (0.075, 13.17), and  $T_{f,[111]}$ (0.088, 16.74) for [001], [011], and [111] loadings, respectively.

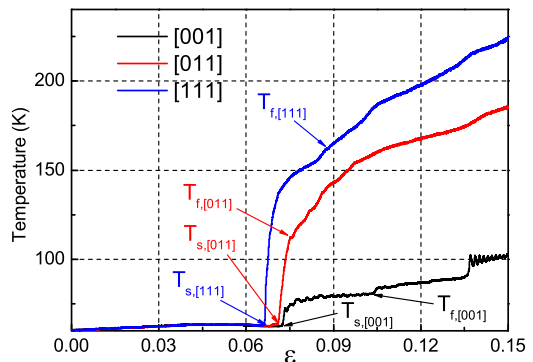


FIG. 2: (Color online) Variation of temperature with the strain  $\epsilon$  for loading along [001], [011], and [111] directions. The letters  $T_{s,i}$  and  $T_{f,i}$  ( $i$  stands for [001], [011], and [111]) have same strains with that in Fig. 1.

## III. RESULTS AND DISCUSSION

### A. Pressure and temperature effects

To begin with, we perform the pressure analysis during the loading process. The calculated pressure as a function of compression strain  $\epsilon$  is shown in Fig. 1, where  $\epsilon=1-V/V_0$  and  $V_0$  is the initial volume of the samples. With increasing the compression strain, the following prominent features can be seen from Fig. 1: (i) The transition critical points in the strain-pressure space are  $T_{s,[001]}$ (0.072, 14.21),  $T_{s,[011]}$ (0.071, 14.66), and  $T_{s,[111]}$ (0.066, 14.16) for loading along [001], [011], and [111] directions, respectively, which illustrates that the critical pressures of transition are less dependent on the crystal orientations. This is similar to the recent shock-loading simulations [13]. However, the strain of  $T_{s,[111]}$  is

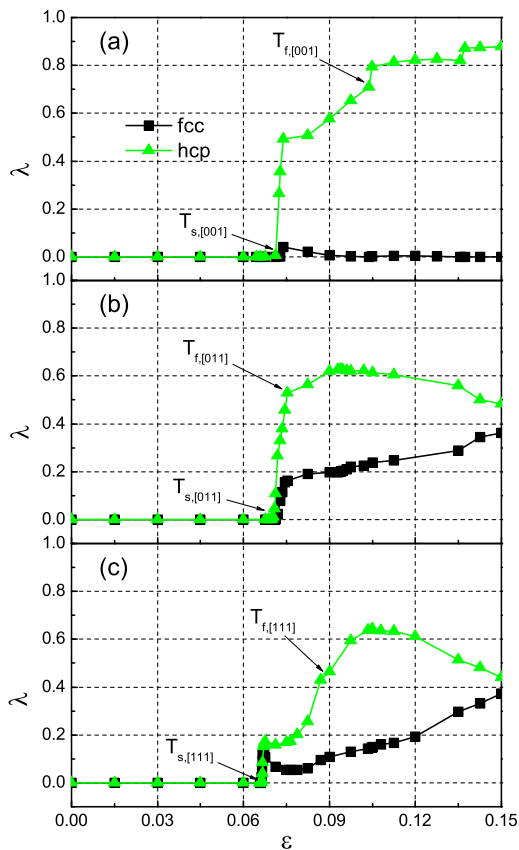


FIG. 3: (Color online) Mass fractions  $\lambda$  for the fcc and hcp phases change with strain  $\varepsilon$  for loading along [001] (a), [011] (b), and [111] (c) directions. The letters  $T_{s,i}$  and  $T_{f,i}$  ( $i$  stands for [001], [011], and [111]) have same strains with that in Fig. 1.

evidently smaller than that of other two critical points, suggesting that sample C begins transition first. After the critical points the pressure is lowered due to the nucleation of the new phases; (ii) Close to the transition critical point  $T_{s,[111]}$ , the pressure-strain curve for [001] loading is below other two curves. This indicates that samples B and C experience a more evident hardening process compared with sample A before phase transition; (iii) The mixed phase intervals are  $T_{s,[001]}$  to  $T_{f,[001]}$ ,  $T_{s,[011]}$  to  $T_{f,[011]}$ , and  $T_{s,[111]}$  to  $T_{f,[111]}$  for loading along [001], [011], and [111] directions, respectively. Obviously, the mixed phase interval in [011] loading is much shorter compared with that in [001] and [111] loadings. This is due to the fact that the compression direction in sample B is parallel to the nucleation planes (see below for further discussion).

Consistent with previous reports [16, 22], in our simulations we have also observed two main steps during structural transition of iron: firstly, atoms in nucleation planes  $\{011\}_{bcc}$  are compressed to form a hexagonal structure; secondly, neighbor  $\{110\}_{bcc}$  layers experience a relative slip to transform into hcp structure.

Under adiabatic compression, the temperature is set free, i.e., not controlled artificially. Thus the temperature evolution with the strain can be calculated based on our data. Results are presented in Fig. 2. One can see that the temperature values at the three starting transition critical points (namely,  $T_{s,[001]}$ ,  $T_{s,[011]}$ , and  $T_{s,[111]}$ ) are all near 64 K, which further implies that the onset of phase transition is insensitive to the loading orientations. Right after the onset of the phase transition, however, loadings along the three different directions display remarkably different temperature effects by the fact shown in Fig. 2 that the temperature is higher one by one with a sequence of [001], [011], and [111] in loading orientation. While the temperatures of samples B and C change up to 185 K and 223 K, the temperature of sample A only increases to 102 K at the end of loading. Also, the temperature increase style is different. The temperature of sample A increases in an up-stair-like manner, which can be seen more carefully near the labels  $T_{s,[001]}$  (0.072, 63.63),  $T_{f,[001]}$  (0.104, 81.17), and followed by a sawtooth-like slope after exceeding the strain of 0.136. Here, the temperature climb up the first stair may contribute to the first step of transition mechanism. This up-stair-like process only costs about 2 ps. Then, the temperature keeps almost no change until the second stair. The second and third stairs in the temperature of sample A have strong relation with the second step in the structural transition of iron. Closer view can find that the temperature fluctuates dramatically after the third stair and only mildly fluctuates after the first two stairs. These features of temperature in sample A has not been observed in samples B and C. Instead, the temperatures in samples B and C first alter suddenly up to 110 K and 142 K from the initial value of  $\sim 64$  K, respectively in 5.3 and 9.3 ps. Then they increase steadily with strain. On the whole, the remarkable distinction in temperature before and after phase transition illustrates the substantial structural and energetic complexity during transition process.

Although the main transition mechanism remains the same for the three kinds of loadings, the details are significantly different. This can be seen from the phase mass fraction analysis. Figures 3(a)-(c) show the mass fraction  $\lambda$  for the hcp and fcc phases during their evolution with the loading strain along the three directions, respectively. In the overall view, the variations of the mass fraction of close packed (fcc/hcp) phases as a function of strain in all three samples are similar to that of temperature. Therefore, the temperature and the nucleation of close packed phases have tight relation. In addition, while most atoms in sample A nucleate into the hcp structure, in samples B and C there will emerge near half proportion of fcc atoms. This is similar to the observation in shock-wave loading simulation [14], where it was found that the hcp/fcc ratio within a grain decreases the more the shock direction deviates from the  $[001]_{bcc}$  direction of the initial polycrystal. In our study, with the pressure increasing, more fcc atoms will form when loading along [011] and [111] directions. The hcp mass fraction decreases with the in-

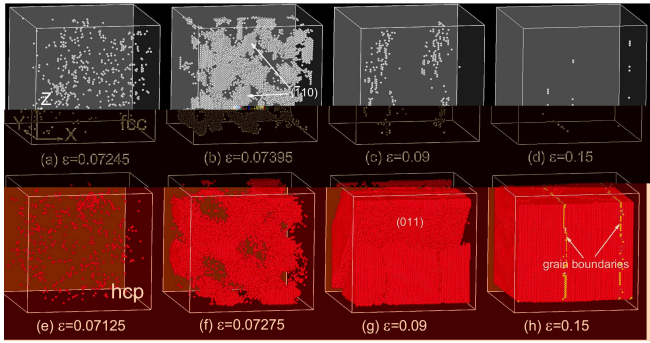


FIG. 4: (Color online) Morphology evolution of the fcc phase (the first row) and the hcp phase (the second row) in sample A with strains labeled under each snapshot. The coordinates are shown in panel (a) and the compression directions is along Z axis. Color coding was obtained by using the topological medium-range-order analysis: white: fcc, red: hcp, yellow: grain boundaries.

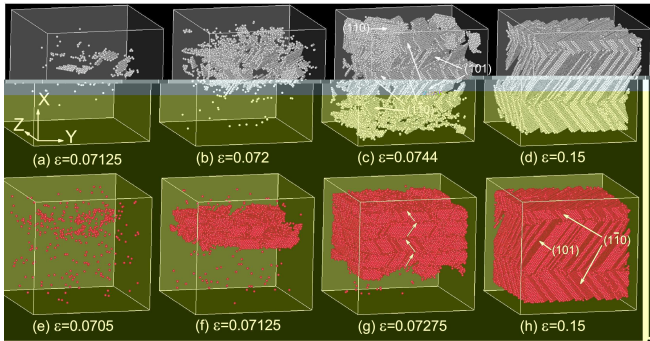


FIG. 5: (Color online) Morphology evolution of the fcc phase (the first row) and the hcp phase (the second row) in sample B with strains labeled under each snapshot. The coordinates are shown in panel (a) and the compression directions is along X axis. Color criterion same with Fig. 4.

crease of fcc phase mass fraction, which indicates that the nucleation of fcc is due to the slip of neighboring hexagonal layers.

## B. Nucleation and growth of hcp and fcc phases

The nucleation and growth of the hcp phase under [001] compression has been investigated in Ref. [17]. Here, we focus on the emergence and growth of both hcp and fcc phases along different crystal directions by continuous uniaxial compression. Over the critical pressure, the close packed phases begin to nucleate in all three kinds of loading. The microscopic view of the initial nucleation and growth of the fcc (upper panels) and hcp (lower panels) phases for samples A, B, and C are shown in Figs. 4-6, respectively. The evolved loading strain corresponding to these snapshots are also labeled. For an overall view, the morphologies of samples A, B, and C are also shown in Fig. 7 at some evolved strains. Based on

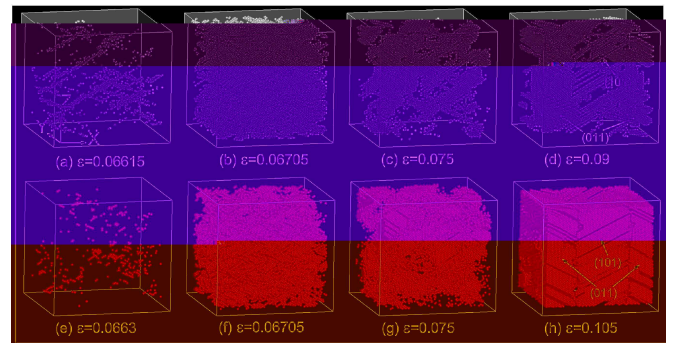


FIG. 6: (Color online) Morphology evolution of the fcc phase (the first row) and the hcp phase (the second row) in sample C with strains labeled under each snapshot. The coordinates are shown in panel (a) and the compression directions is along Z axis. Color criterion same with Fig. 4.

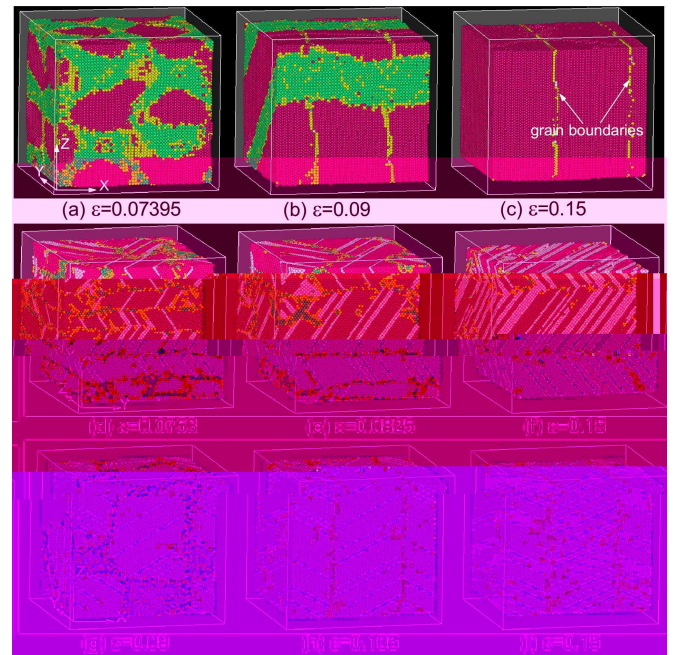


FIG. 7: (Color online) Compressed samples under different strains with the first row (three snapshots) for [001] loading, the second row for [011] loading, and the third row for [111] loading. The compression directions of all samples are from top to bottom. The coordinates are shown in (a), (d) and (g) for loading along [001], [011], and [111] directions, respectively. The green atoms stand for the bcc structure and other color criterion same with Fig. 4.

these figures, we can clearly see that for the [001] and [111] loadings, until strain being loaded up to 0.09, the bcc structure atoms still maintain bulk morphology, as shown in Fig. 7(b) and 7(g). For the loading along [011] direction, on the contrary, only a few bcc atoms dispersively distribute among bulk hcp and fcc atoms when the loaded strain is over 0.075. This further implies that the

mixed phase interval in sample B is shorter than in other two samples.

For the [001] loading, as shown in Fig. 4, some fcc-phase atoms only appear in mixed phase interval and nucleate on  $(\bar{1}10)_{\text{bcc}}$  plane. With increasing pressure, the fcc atoms will transform to hcp or grain boundary atoms. From Fig. 4(d), we can find that a little amount of fcc atoms appear only in the twin boundaries. For hcp atoms, initially, they homogeneously nucleate [Fig. 4(e)], then evolve into irregular grains [Fig. 4(f)]. These grains subsequently develops into the typical laminar structure along the  $(011)_{\text{bcc}}$  planes, as shown in Fig. 4(g). Ultimately, the laminar structure grows into larger and regular grains divided by the grain boundaries [Fig. 4(h)]. The grain boundary planes are  $(100)_{\text{bcc}}$  planes, paralleling with the compression direction.

While loading along [011] (see Fig. 5), the fcc phase nucleates on  $(110)_{\text{bcc}}$ ,  $(101)_{\text{bcc}}$ , and  $(\bar{1}\bar{1}0)_{\text{bcc}}$  planes and the hcp on  $(101)_{\text{bcc}}$  and  $(110)_{\text{bcc}}$  planes. These nucleation planes all belong to the  $\{110\}_{\text{bcc}}$  family. More specially, the fcc atoms first nucleate as a flaky structure [Fig. 5(a)], then, together with hcp atoms, evolve into the thin sandwich structure perpendicular to the compression direction [see Fig. 5(b), 5(c), 5(f), 5(g), and Fig. 7(d)]. At the end of loading, the fcc and hcp atoms form stacking fault structure and relatively thick sandwich structure [Fig. 5(d) and 5(h)]. Therein, the sandwich structure is divided by the grain boundaries, which can be more clearly seen from the yellow atoms in Fig. 7. Note that the grain boundary planes are  $(011)_{\text{bcc}}$  planes and perpendicular to the compression direction.

For loading along [111] (see Fig. 6), the nucleation and growth of the close packed phases are different. Just over the critical pressure, both fcc and hcp atoms nucleate to form lots of small but long flaky structure [Fig. 6(a), 6(b), 6(e), and 6(f)]. From Fig. 3(c), a relaxation process right after the critical point  $T_{s,[111]}$  has been observed. Although the fractions of fcc and hcp phases are reduced, the arrangement of atoms becomes more inerratic, as shown in Fig. 6(c) and 6(g). At the end of loading, the stacking fault arrangement comes out in the interior of thick sandwich structure. Compared to the [011] loading, both fcc and hcp nucleation crystalline planes in [111] loading are  $(101)_{\text{bcc}}$  and  $(011)_{\text{bcc}}$ . Besides, the grain boundary planes  $(\bar{1}\bar{1}0)_{\text{bcc}}$  in [111] loading are parallel, instead of perpendicular (in the case of [011] loading), to the compression orientation.

On the whole, for [001] loading, the  $\alpha \rightarrow \epsilon$  transition happens in the whole body of the sample and fcc structure only appears as the intermediate structure. However, for [011] and [111] loadings, the fcc and hcp structures nucleate simultaneously. Note that for [011] loading the nucleation is localized. The hcp structure reaches its maximum at the evolved strain of  $\sim 0.09$  and  $\sim 0.1$  for [011] and [111] loadings, respectively. Further increase of strain will result in the decrease (increase) of hcp (fcc) weight. A visible difference between [011] and [111] loadings is that for the latter, there occurs an evident relax-

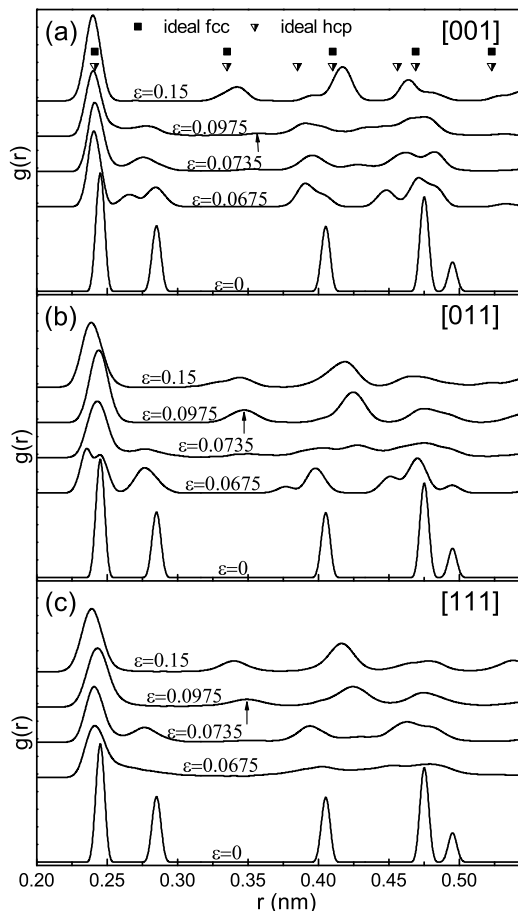


FIG. 8: Radial distribution functions (RDFs) under different strains  $\epsilon$  for crystals compressed along [001] (a), [011] (b), and [111] (c) directions. As a reference the ideal positions of the fcc and hcp structures, as well as the distribution function for the unstrained bcc ( $\epsilon=0$ ), are shown.

ation process after the critical point.

### C. Radial distribution function analysis

The slip investigation of atoms must presume upon radial distribution function (RDF) analysis and phase mass fraction analysis. Figure 8 displays the RDFs under different compressions, where the strains of all three samples are from 0 to 0.15. The ideal positions of fcc and hcp structures have also been plotted. Along with the increase of strain the first peak in all three samples deviates towards left gradually, while the second peak deviates towards the first peak and disappears finally. After the strain becomes bigger than 0.0975, along with the disappearance of the second peak, a new peak appears, with the position (shown by the arrows in Fig. 8) exactly the same as that of the second peak of the fcc/hcp phases. Therefore, these changes in RDFs definitely signify atomic transformation to the close packed phases.

Moreover, the evident broadening of the peaks in [011] and [111] loadings after transition is caused by the temperature effect. The third and fourth peaks at  $\varepsilon=0.15$  in Fig. 8(a) obviously trend to split; this is prominently different from that in Figs. 8(b) and 8(c). This further illustrates that sample A is mainly featured by the hcp phase at the end of loading. All these analyses indicate that the phase distribution and the mechanism of local slip in three samples are different in the details of transition process.

#### IV. CONCLUSIONS

In summary, we have simulated the process of  $\alpha \rightarrow \epsilon/\gamma$  structural phase transition in bcc single crystal iron under uniaxial compression along three typical bcc orientations by MD method. It is found that samples B and C experience a more evident hardening process compared with sample A before phase transition. The temperatures for [011] and [111] loadings increase more highly than that for [001] loading. The mixed phase interval of sample B is much shorter than other two samples, which is caused by the fact that the compression orientation belongs to the nucleation planes  $\{110\}_{\text{bcc}}$ . The transition

pressure is the same for all three samples with a value of  $\sim 14$  GPa, over which the nucleation of hcp and fcc atoms appears and grows into different morphologies. For [001] loading, the  $\alpha \rightarrow \epsilon$  transition happens in the whole body of the sample and hcp atoms nucleate on  $(011)_{\text{bcc}}$  planes to form laminar structure; the fcc phase only appears intermediately. For [011] and [111] loadings, however, (i) nucleation of fcc and hcp structures occurs simultaneously; (ii) the hcp mass fraction reaches its maximum at the evolved strain of  $\sim 0.09$  and  $\sim 0.1$  and further increase of strain will result in the decrease (increase) of hcp (fcc) weight; (iii) the fcc and hcp atoms form stacking fault structure and relatively thick sandwich structure at the end of loading. Note that for [011] loading the nucleation is localized. The phase distribution and the mechanism of local slip in three samples are different in detail.

#### Acknowledgments

This study has been supported by the Foundations for Development of Science and Technology of China Academy of Engineering Physics under Grants No. 2008B0101008.

- 
- [1] D. Bancroft, E. L. Peterson, and S. Minshall, *J. Appl. Phys.* **27**, 291 (1956).
  - [2] Jamieson and A. W. Lawson, *J. Appl. Phys.* **33**, 776 (1962).
  - [3] L. M. Barker and R. E. Hollenbach, *J. Appl. Phys.* **45**, 4872 (1974).
  - [4] R. D. Taylor, M. P. Pasternak, and R. Jeanloz, *J. Appl. Phys.* **69**, 6126 (1991).
  - [5] H. Hasegawa and D. G. Pettifor, *Phys. Rev. Lett.* **50**, 130 (1983).
  - [6] J. C. Boettger and D. C. Wallace, *Phys. Rev. B* **55**, 2840 (1997).
  - [7] F. M. Wang, and R. Ingalls, *Phys. Rev. B* **57**, 5647 (1998).
  - [8] K. J. Caspersen, A. Lew, M. Ortiz, and E. A. Carter, *Phys. Rev. Lett.* **93**, 115501 (2004).
  - [9] K. Kadau, T. C. Germann, P. S. Lomdahl, and B. L. Holian, *Science* **296**, 1681 (2002).
  - [10] M. S. Daw and M. I. Baskes, *Phys. Rev. Lett.* **50**, 1285 (1983).
  - [11] M. S. Daw and M. I. Baskes, *Phys. Rev. B* **26**, 6443 (1984).
  - [12] D. H. Kalantar, J. F. Belak, G.W. Collins, J. D. Colvin, H. M. Davies, J. H. Eggert, T. C. Germann, J. Hawreliak, B. L. Holian, K. Kadau, P. S. Lomdahl, H. E. Lorenzana, M. A. Meyers, K. Rosolankova, M. S. Schneider, J. Sheppard, J. S. Stölken, and J. S. Wark, *Phys. Rev. Lett.* **95**, 075502 (2005).
  - [13] K. Kadau, T. C. Germann, P. S. Lomdahl, and B. L. Holian, *Phys. Rev. B* **72**, 064120 (2005).
  - [14] K. Kadau, T. C. Germann, P. S. Lomdahl, and B. L. Holian, *Phys. Rev. Lett.* **98**, 135701 (2007).
  - [15] B. Yaakobi, T. R. Boehly, D.D. Meyerhofer, T. J. B. Collins, B. A. Remington, P. G. Allen, S. M. Pollaine, H. E. Lorenzana, and J. H. Eggert, *Phys. Rev. Lett.* **95**, 075501 (2005).
  - [16] X. Cui, W. Zhu, H. He, X. Deng, and Y. Li, *Phys. Rev. B* **78**, 024115 (2008).
  - [17] J. L. Shao, S. Q. Duan, A. M. He, C. S. Qin, and P. Wang, *J. Phys.: Condens. Matter* **21**, 245703 (2009).
  - [18] R. Harrison, A. F. Voter, and S. P. Chen, in *Atomistic Simulation of Materials*, edited by V. Vitek and D. J. Srolovitz (Plenum, New York, 1989), p. 219.
  - [19] K. H. Hoffmann, *Computational Physics* (Springer-Verlag, Berlin Heidelberg, 1996), p. 268
  - [20] W. C. Swope, H. C. Andersen, P. H. Berens and K. R. Wilson, *J. Chem. Phys.* **76**, 637 (1982).
  - [21] J. D. Honeycutt and H. C. Andersen, *J. Phys. Chem.* **91**, 4950 (1987).
  - [22] J. Hawreliak, J. D. Colvin, J. H. Eggert, D. H. Kalantar, H. E. Lorenzana, and J. S. Stölken, H. M. Davies, T. C. Germann, B. L. Holian, K. Kadau, and P. S. Lomdahl, A. Higginbotham, K. Rosolankova, J. Sheppard, and J. S. Wark, *Phys. Rev. B* **74**, 184107 (2006).